Heterogeneous silicon mesostructures for lipid-supported bioelectric interfaces

Yuanwen Jiang[1,2,*], **João L. Carvalho-de-Souza**[3,*], **Raymond C. S. Wong**[2,3,*], **Zhiqiang Luo**[1,2], **Dieter Isheim**[4,5], **Xiaobing Zuo**[6], **Alan W. Nicholls**[7], **Il Woong Jung**[8], **Jiping Yue**[9], **Di-Jia Liu**[10], **Yucai Wang**[1,2], **Vincent De Andrade**[6], **Xianghui Xiao**[6], **Luizetta Navrazhnykh**[1], **Dara E. Weiss**[1], **Xiaoyang Wu**[9], **David N. Seidman**[4,5], **Francisco Bezanilla**[3,11,†], and **Bozhi Tian**[1,2,11,†]

[1]Department of Chemistry, the University of Chicago, Chicago, IL 60637

[2]The James Franck Institute, the University of Chicago, Chicago, IL 60637

[3]Department of Biochemistry and Molecular Biology, the University of Chicago, Chicago, IL 60637

[4]Department of Materials Science and Engineering, Northwestern University, Evanston, IL 60208

[5]The Northwestern University Center for Atom-Probe Tomography (NUCAPT), Northwestern University, Evanston, IL 60208

[6]The X-ray Science Division, Argonne National Laboratory, Argonne, IL 60439

[7]The Research Resources Center, University of Illinois at Chicago, Chicago, IL 60607

[8]The Center for Nanoscale Materials, Argonne National Laboratory, Argonne, IL 60439

[9]Ben May Department for Cancer Research, the University of Chicago, Chicago, IL 60637

[10]The Chemical Sciences and Engineering Division, Argonne National Laboratory, Argonne, IL 60439

[11]The Institute for Biophysical Dynamics, the University of Chicago, Chicago, IL 60637

Abstract

Silicon-based materials have widespread application as biophysical tools and biomedical devices. Here we introduce a biocompatible and degradable mesostructured form of silicon with multiscale

---

structural and chemical heterogeneities. The material was synthesized using mesoporous silica as a template through a chemical-vapor-deposition process. It has an amorphous atomic structure, an ordered nanowire-based framework, and random submicrometre voids, and shows an average Young's modulus that is 2–3 orders of magnitude smaller than that of single crystalline silicon. In addition, we used the heterogeneous silicon mesostructures to design a lipid-bilayer-supported bioelectric interface that is remotely controlled and temporally transient, and that permits non-genetic and subcellular optical modulation of the electrophysiology dynamics in single dorsal root ganglia neurons. Our findings suggest that the biomimetic expansion of silicon into heterogeneous and deformable forms can open up opportunities in extracellular biomaterial or bioelectric systems.

Silicon (Si) is a widely used material in biomedical research[1–11] because it is biocompatible and biodegradable, and it exhibits a spectrum of important electrical, optical, thermal and mechanical properties. For example, Si-based systems can sense electrical activities of the brain in flexible and adhesive configurations[12–14], deliver nucleic acids *in vivo* to induce angiogenesis[7], and perform intra- and intercellular force dynamics measurement[15]. So far, most of the applications of Si as biomaterials have been focused on or originated from single crystalline structures or substrates, which is primarily due to the need for high quality and controllable electrical or other properties. New Si-based forms that are unique in composition, structure, and property have the potential to yield nontraditional applications for Si-based biomaterials and open up unexpected new avenues for research and device manufacturing.

Structural heterogeneity

Natural biomaterials have remarkable diversity in structure and function and may guide the design[16] of new Si forms[17–22] for subcellular interfaces and biophysical modulation (Fig. 1a). Given this hypothesis, we first focused on the synthesis of three-dimensional (3D) Si-based biomaterials with an ordered and uni-directionally aligned fibril-based framework (Fig. 1a); we did so because this layout is fundamental to many natural biomaterials[16,23] (*e.g.*, bone[16]) and extracellular matrices (ECM)[24]. We employed a nano-casting approach[17,25–28] with ordered hexagonal mesoporous silica (SiO$_2$) SBA-15[29] as the template, in which silane (SiH$_4$) decomposition inside the channels and pores could provide the nanowire arrays with self-supporting micro-bridges[25,26]. While nano-casting synthesis of mesoporous solids is highly versatile and scalable, ordered and freestanding Si-based mesostructures with molecular-level principal feature sizes (*i.e.*, < 10 nm) are still challenging to achieve[17,18,27,30]. We designed a chemical vapor deposition (CVD) apparatus with a double-quartz-tubing system (Supplementary Fig. S2) in which the SiO$_2$ template (SBA-15) was placed near the bottom of the inner tube (Figs. 1b and S1). We have identified an optimal growth temperature at 500 °C (Supplementary Fig. S3) with a duration of 2h (Supplementary Fig. S4), when 200 mg of SBA-15 template was used. After CVD, subsequent wet chemical etching with hydrofluoric acid (HF) removed the SiO$_2$ and yielded a brownish powder (Fig. 1b). The scanning electron microscopy (SEM) image shows wheat-like aggregates with individual grain width of ~2 μm (Fig. 1c). The size or morphology uniformity can be improved by using shape-controlled SBA-15 templates (*e.g.*, rod-like or

spherical shapes, Supplementary Figs. S5 and S6), or adopting post-synthesis separations (Supplementary Fig. S7). The freshly etched and dried Si-based samples did not result in combustion upon xenon flash illumination or mechanical grinding, suggesting that the mesostructured Si surfaces are ignition-resistant in air[1]. The sample is electrically conductive, and single particle measurements yielded a representative electrical conductance of 2.4 μS (Supplementary Fig. S8). The powder can be molded and embossed like clay (Supplementary Fig. S9a), dispersed as a suspension and drop-casted to form thin films (Supplementary Fig. S9b), and injected and retained locally within collagen hydrogel (Supplementary Fig. S9c).

Nano-computed tomography (nano-CT) from transmission X-ray microscopy (TXM) measurement reveals that individual particle aggregate contains random micron- and sub-micron scale inter- or intra- (blue) granular voids (Fig. 1d), reminiscent of the cavities in spongy bones. The voids have a total volume fraction of 0.7% (intra-)/50.0% (inter-) and width of ~0.2–2 μm (Supplementary Fig. S10b), likely formed through the diffusion-limited incomplete filling of Si inside mesoporous SiO_2.

A small angle X-ray scattering (SAXS) profile (Fig. 1e) exhibits diffraction peaks indexed as (100), (110) and (200) of a two-dimensional hexagonal structure (space group, $p6mm$), as expected from the SBA-15 template[29]. The lattice constant a calculated from SAXS was 11.1 nm, which is consistent with that of the SiO_2 template (11.0 nm) and suggests a faithful replication. The Brunauer-Emmett-Teller (BET) specific surface area and total pore volume as measured by N_2 sorption were 462 m^2/g and 0.53 cm^3/g, respectively (Supplementary Fig. S10a).

The high-resolution SEM shows assemblies of aligned nanowires within individual grains (Fig. 1f), as expected from the channel structures in SBA-15 template. The end-view transmission electron microscopy (TEM) image and the fast Fourier transform (FFT) diffractogram (Fig. 1g) confirm the hexagonally ordered packing of nanowires (Supplementary Fig. S10c). Selected area electron diffraction (SAED) shows diffuse rings and indicates that Si is amorphous (Fig. 1g), a useful property for improving light absorption[31] and reducing rigidity[32] in Si (Table S1). *In-situ* heating experiments with both TEM (Supplementary Fig. S11) and SAXS (Supplementary Fig. S12) showed that the ordered mesostructures remained at 900 °C for at least 2 hours, although partial crystallization was observed (Supplementary Fig. S11). Finally, this synthetic approach is generalizable to other Si frameworks, *e.g.*, a gyroidal lattice with a space group of $Ia\overline{3}d$ (Supplementary Fig. S13).

Chemical heterogeneity

The high-angle annular dark-field scanning transmission electron microscopy (HAADF STEM) image highlights individual nanowires (Supplementary Fig. S14a), whose ordered packing suggests the existence of interconnecting micro-bridges[25,26]. Energy dispersive X-ray (EDX) mapping of one representative area shows an alternating distribution of oxygen (O) and Si (Supplementary Fig. S14b). Because a long etching time (5–10 min in HF) was adopted to remove the SiO_2 template, and given the large pore volume (*i.e.*, 0.53 cm^3/g)

exhibited by the material, the O signals came primarily from the oxidized portions in the Si open framework instead of from the SiO_2 template residuals.

To quantitatively determine the heterogeneous O distribution, we used atom probe tomography (APT) to obtain elemental distributions in a Si framework with sub-nanometer scale spatial resolution (Figs. 2, S15, S16). A reconstructed 3D dataset (Figs. 2a, S16), collected from one Si particle with an intact SiO_2 template (*i.e.*, without dissolving SiO_2 by HF), displayed a hexagonal arrangement of nanowires with a lattice constant of 10.7 nm, consistent with the SAXS and TEM results (Fig. 1). Additionally, individual micro-bridges can be readily visualized (Fig. 2b, yellow arrow), and statistical analyses (*n*=34) demonstrated that the angles between a micro-bridge and its adjacent nanowires peaked at ~90° (Supplementary Fig. S16b). Given this quasi-orthogonal arrangement between nanowires and micro-bridges, we were able to isolate two components in orthogonal thin slices (Fig. 2c).

Next, we studied the distribution of Si and O atoms with isoconcentration surface analysis (Fig. 2b). The results demonstrate that although the interconnecting micro-bridges are visible in the 60 at.% Si isoconcentration surface map (Fig. 2b, upper panel), most of them no longer appear in the 75 at.% one (Fig. 2b, lower panel), indicating that the overall Si (O) concentration is less (more) in the micro-bridges. We further analyzed the proximity histogram concentration profile averaged over the selected region (Fig. 2d). Because the micro-bridges have smaller diameters than nanowires (*i.e.*, < 2 vs. ~7 nm), Si oxidation due to O incorporation from the SiO_2 template or air places the Si concentration generally below 75 at.% in micro-bridges (Fig. 2d, thick pink line). Moreover, this Si concentration difference can be quantified using a concentration distribution histogram derived from isoconcentration surface analysis within the two slices (Fig. 2e), which displays distinct distributions in each domain (< 75 at.% for micro-bridges, < 95 at.% for nanowires) (Fig. 2e). Finally, the Si concentration in the template (*i.e.*, SiO_2 regions that are away from the Si/SiO_2 interface) was ~43 at.% (Fig. 2d), higher than that in pure SiO_2 (*i.e.*, 33 at.%). This suggests that silane decomposition can also occur inside sub-nanometer cavities within the mesoporous SiO_2 walls, confirming a domain previously proposed as microporous 'corona'[33]. Taken together, the electron microscopy (Figs. 1f, 1g and S14), EDX (Supplementary Fig. S14) and APT (Figs. 2, S16) demonstrate that the Si framework exhibits a chemical heterogeneity, where amorphous Si constitutes most of the nanowire-based component and the thinner micro-bridges have an overall higher O concentration and integrates the nanowires (Fig. 2f).

Mechanical properties

We then explored the physical properties related to the observed structural and chemical heterogeneities. Given their critical role in establishing minimally invasive biointerfaces[3,34,35], we first studied the mechanical properties. In a dry state, the Si framework showed an average Young's modulus of 1.84 GPa (Fig. 3a), which is ca. 2 and 1 orders of magnitude smaller than that for bulk Si (~180 GPa) and electrochemically etched porous Si with similar porosity (~20 GPa)[1], respectively. This significant reduction in modulus is likely a combined result of multi-scale porosity, an amorphous framework, the

molecular-level feature sizes of both nanowires and the micro-bridges, and the chemical heterogeneity as identified by APT (Figs. 2d, 2e).

After being immersed in a phosphate-buffered saline (PBS) solution for ~2 hours, the average Si Young's modulus decreased to 0.41 GPa (Fig. 3a), comparable to that of hydrated collagen fibers[36] and only 1 order of magnitude larger than that of phospholipid bilayers[37]. This reduction of modulus may come from framework degradation in saline, especially through the O-rich micro-bridges that maintain the framework integrity. However, *in-situ* and *ex-situ* SAXS (Supplementary Fig. S17) show that ordered mesostructures dominate in the remaining insoluble material for at least two days at room temperature in both PBS and collagen hydrogel. Cross-sectional TEM also shows long-range order in the interior of these saline treated samples (Supplementary Fig. S18a), although partially-degraded nanowire segments can be observed (Supplementary Fig. S18b). Raman and ultraviolet-visible (UV-vis) spectra indicate that the remaining Si materials displayed marginal changes in their atomic structures (*i.e.*, the characteristic transverse optical Raman peak position and width, correlating with the spread in mean Si-Si-Si bond angle[38], remain at ~480 cm^{-1} and ~59 cm^{-1}) and optical properties (*e.g.*, the optical band gap) after being immersed in PBS for 1 day (Figs. 3b, 3c). These results suggest that the interior of the Si mesostructures were preserved, and that the measured modulus reduction in saline is likely a result of degradation of particle surfaces. Indeed, we have observed surface accumulation of degradation products in a confined space, *e.g.*, a cavity from a piece of wrapped human umbilical vein endothelial cell (HUVEC) membrane (Supplementary Fig. S18c). Overall, this degradation pathway is surface-initiated, instead of being bulk degraded (as usually expected for water-permeable nanoporous materials). We attribute this behavior to the possible blockage of molecular-level pores by the partially-degraded products (*i.e.* gel-like $Si_xO_y(OH)_z^{4x-2y-z}$) over particle surfaces (Supplementary Fig. S19), which may delay the disruption of the internal ordered framework in saline — as seen in both SAXS and TEM (Supplementary Figs. S17, S18). Finally, mesostructured Si can completely degrade[10,11] in saline over time and its behavior is dependent on multiple factors, such as initial Si/water ratio, solution exchange protocol, and temperature (Supplementary Fig. S20).

Close inspection at the Si/HUVEC interfaces reveals a minimum of ~ 30 nm wide space between the ordered domains of Si particle and the plasma membrane (Figs. 3d), likely filled with degraded Si that is more deformable (Fig. 3a) and natural ECM. Additionally, we observed little correlation between the nanowire orientation and the cell surfaces, as shown in samples prepared with both freeze-substitution (Fig. 3d) and chemical fixation (Supplementary Fig. S18) methods, suggesting that nanoscale surface topography from Si particle may not be critical for establishing stable biointerfaces.

Biocompatibility

To evaluate the biological benefit of using mesostructured Si, we developed a single cell calcium-imaging assay in which fluorescence dynamics were recorded upon pressing vertically on a HUVEC cell-supported Si particle (size: ~ 5 μm) with a glass micropipette (Fig. 3e). Compared to grinded single crystalline Si particles, mesostructured Si yields statistically smaller values in both amplitude (F/F_0) and slope (($dF/dt)/F_0$) in the

mechanically-induced calcium dynamics curves (Figs. 3e, S21). These single cell studies confirm that deformable materials are less invasive to cellular components[3]. Finally, mesostructured Si yielded negligible cytotoxicity in several mammalian cell cultures (Supplementary Fig. S22). And when tested in rats subcutaneously, the inflammatory response that was caused by injection and the materials decreased substantially from 1-day to 3-week time points as mesostructured Si degraded (Supplementary Fig. S23).

Bioelectric interfaces

Altogether, this biocompatible and degradable form of Si has intrinsic (*i.e.*, as grown, Figs. 1 and 2) and induced (*e.g.*, by water, Fig. 3) chemical and structural heterogeneities, despite its origin from a single Si precursor (*i.e.*, SiH_4). Given that these heterogeneities are spatially organized and seamlessly integrated, a single particle may exhibit multiple functions (Supplementary Fig. S19), a scenario similar to that in natural biominerals[16,39]. For example, we expect good photothermal efficacy from the interior of the Si mesostructures (Supplementary Fig. S19) due to enhanced intrinsic light absorptivity in amorphous Si[31], and reduced thermal conductivity and capacity as previously demonstrated for porous Si[1]. Taking advantage of the fact that a rapid temperature variation can induce transient capacitive currents in phospholipid bilayers[40,41] (see Supplementary Text), we constructed a hybrid Si/phospholipid system as a remotely controlled bioelectric interface (Fig. 4a, left). A layer of grinded Si mesostructures (individual particle size: ~ 1–2 μm, Supplementary Fig. S7a) was supported over one side of a phospholipid bilayer, and its local junction with lipids was remotely actuated with 532 nm laser pulses (laser beam diameter: ~ 40 μm; Figs. 4b, S24). We measured the temperature change near the mesostructured Si layer using a calibrated micropipette resistance method[40]; we simultaneously assessed the electrical capacitance dynamics with the impedance method[40] using a sinusoidal voltage (Fig. 4b). Next, we recorded membrane current dynamics under voltage-clamp mode (Fig. 4b; see details in Supplementary Information). Experiments and finite element analysis simulation revealed a fast photothermal effect (Fig. 4c, upper panel; Supplementary Figs. S24 and S25), and such a fast response is critical for capacitive current generation in lipid bilayer[40]. For example, one 11.2 μJ laser pulse causes a ~5.8 K increase of local temperature within 1.8 ms, followed by a decay to baseline with ~2.2 ms time constant (Fig. 4c, upper panel). With the same pulse, the estimated capacitance change accompanying the fast temperature rise peaks at ~0.6 % (Fig. 4c, lower panel). Because impedance correlates inversely to capacitance, a fast increase in bilayer capacitance due to laser pulses leads to a reduction of impedance, and correspondingly, a light-induced transient membrane current. Such a membrane current is capacitive and depolarizing (*i.e.*, current flow tends to reduce the polarization in the phospholipid bilayer); its amplitude is tunable with either laser input energy (Supplementary Fig. S24) or a voltage drop across the bilayer (Fig. 4d). Because both the membrane current output and the local temperature variation are transient, this Si/bilayer platform may be adapted for minimally invasive and dynamic biomaterials or devices.

To investigate this possibility, we proposed a dynamic hybrid Si/cell system (Figs. 4a and 4e) where individual mesostructured Si particles attached to dorsal root ganglia (DRG) neurons, with 532 nm laser pulses and intracellular electrical recordings as input and output,

respectively (see Supplementary Information). We prefer to use individual micron-scale and thermally stable (Figs. S11 and S12) Si mesostructures over ensembles of existing nanoparticles[41] in order to achieve efficient and point-like localized extracellular control, as well as to avoid material internalization by neurons[42] or laser heating-induced particle change[43]. By varying the laser stimulation duration while fixing its wavelength and power (532 nm, 5.32 mW, beam diameter: ~ 10 μm), we identified an average of 5.32 μJ (Supplementary Fig. S26a) threshold energy for reliably eliciting single action potentials (AP) in DRG neurons with a singly attached Si particle (particle size: ~ 2 μm). This energy level is ~30× less than those used for a recently reported precise neuromodulation with Au nanoparticles[41]. Given the experiments on phospholipid bilayers (Figs. 4b, 4c and 4d) and the controls with mesoporous SiO_2 (Supplementary Fig. S27), under current-clamp conditions, the fast and transient photothermal effect from the Si framework (Supplementary Fig. S24) induces depolarization that opens sodium channels thus triggering APs. Since neurons process information *via* spike trains, we mimicked this process by delivering trains of 5.32 μJ laser pulses with different frequencies. We demonstrated reproducible and precise optical stimulation up to 15 Hz (Fig. 4f, upper left). At higher frequencies, AP generation becomes less efficient, although a deterministic sub-threshold depolarization remains evident (Supplementary Fig. S26b). After reaching 20 Hz, *e.g.*, at 25 Hz (Fig. 4f, middle), the neural stimulation efficacy declined, response time (spike latency) and its standard deviations (trial-to-trial jitter and throughout train jitter, see Materials and Methods) increased (Supplementary Fig. S26c), all of which are most likely limited by the intrinsic ion channel kinetics (Fig. 4a, right)[40,44]. Interestingly, at 30 Hz input, the real-time electrical recording trace shows a quasi-alternating pattern of APs and sub-threshold depolarization (Fig. 4f, lower left). Accordingly, fast Fourier transform of the time-dependent trace shows a splitting distribution in the frequency domain (Fig. 4f, lower right), one at half-input frequency (for APs) and the other at the original input frequency (for sub-threshold depolarization). This emergent output behavior results from dynamic feedback[44] among Si-induced thermal and ionic effects, ion channel activities and membrane potentials (Fig. 4a, right). A return map analysis (Figs. 4g and S28, A_n-A_{n+1}, A_n is the area of the nth induced neuronal signal)[44] shows frequency dependent 2-D patterns, being either focused (*e.g.*, 15 Hz) or partitioned/diffused (*e.g.*, 30 Hz), suggesting another mechanism for output recognition.

Outlook

Future efforts include systematic control of the position and efficacy of Si/cell interfaces and demonstration of more complex dynamic behaviors in the hybrid system. These are feasible given that individual mesostructured Si particles can be positioned in an arbitrary manner by a glass micropipette (Supplementary Fig. S29), that Si particles can be patterned as a micro-pad array over centimeter-scale area by photolithography (Supplementary Fig. S30), and that size- and shape-controlled preparation of Si particles is achievable (Supplementary Figs. S5, S6, S7). Additionally, tools such as light-emitting diode and calcium imaging can be explored for stimulation and recording of neural activities, which would be beneficial for *in vivo* studies.

Existing materials, such as particles of single crystalline silicon or carbon, may be configured into similar interfaces, although they do not currently exhibit the deformability or degradability desired for biomaterials. Hydrogels and polymers[45,46] are softer and may form mechanically compliant interfaces for similar studies, however appropriate chemical designs are needed for achieving both degradability and fast photothermal dynamics (*e.g.*, a few degrees of temperature increase within milliseconds). Regardless of exploring other materials, the current demonstrations of lipid bilayer-level integration of a bioelectric interface and the hybrid cellular system suggest that it may be possible to use amorphous Si, a much less exploited material in biomedical research, as a building block in establishing functional bio-interfaces[13,35,47–49] and as a new bio-orthogonal and dynamic component for future synthetic biology[50].

Methods

Synthesis of mesostructured Si

Mesostructured Si was prepared by CVD of Si inside mesoporous SiO_2, followed by HF etching to remove the template. Si was deposited at 500 °C and 40 Torr using silane as the Si precursor and hydrogen as the carrier gas. In a typical synthesis, we used 200 mg of SiO_2 template, with flow rates of H_2 and SiH_4 set at 60 and 2 standard cubic centimeters per minute, and a total CVD duration of 120 min. Subsequent HF etching for 5–10 min was used to remove the template at room temperature.

Structural characterizations

SAXS measurements were conducted at the 12ID-B station at the Advanced Photon Source (APS), Argonne National Laboratory (ANL). TXM nano-CT was performed on the new transmission X-ray microscope at sector 32-ID of APS in ANL. SEM was performed on a Merlin FE-SEM (Carl Zeiss, Germany). TEM and SAED were done using a Tecnai F30 TEM (FEI, USA).

Atom-probe tomography (APT)

The APT was run in an ultraviolet (UV) laser-assisted local-electrode atom-probe (Cameca, USA, LEAP 400XSi). Surface atoms from a microtip were evaporated with an applied voltage of 1~6 kV and the assistance of a 30 pJ UV (wavelength λ=355 nm) laser pulsing at 250 kHz frequency. The samples were held at 30 K and 2×10^{-11} Torr during APT experiments. The 3D reconstructions and data analyses were performed using Cameca's Integrated Visualization and Analysis Software (IVAS) 3.4 code.

Atomic force microscopy (AFM) measurements

Force curves were collected using an Asylum MFP-3D AFM (Asylum Research, USA) with ACTA (AppNano, USA, nominal spring constant 40 N/m) probes in air and AC240 (Olympus, Japan, nominal spring constant 2 N/m) probes in liquid. Prior to solution phase AFM experiments, samples were also soaked in 1× PBS solution at room temperature for ~2 h. Force curves were recorded by loading at a rate of 1μm/s up to an indentation depth of ~10 nm, followed by unloading at the same rate.

UV-vis and Raman spectroscopy

Diffuse reflectance UV-Vis spectra were collected on a Cary 5000 UV-Vis-NIR spectrometer (Varian, USA) equipped with a diffuse reflectance accessory (DRA). Raman spectra were recorded using a LabRAM HR evolution system (Horiba, Japan).

Cell/Si interfaces imaging

HUVEC/Si mixtures were either frozen under high pressure and freeze-substituted or chemically fixed before epoxy resin embedding. Epoxy sections of ~100 nm were cut using an ultramicrotome and collected on copper grids for imaging on a Tecnai F30 TEM (FEI, USA).

Calcium imaging

HUVECs were stained with Fura-2 AM and washed with a HEPES-buffered Tyrode's solution. Mesostructured and solid Si particles have similar lateral sizes of ~5 μm. Particles sitting on cell bodies were pushed by glass micropipettes controlled by a micromanipulator. After making contact with the particles, pipettes were lowered by another 1 μm and held still for 20 s before retraction. During the whole process, fluorescence images were collected using an upright microscope (BX61WI, Olympus, Japan) equipped with an EM-CCD camera (C9100-13, Hamamatsu Photonics, Japan).

Artificial lipid bilayer experiments

A custom-made upper chamber containing a 300 μm diameter hole for planar lipid bilayer (asolectin lipids, soybean polar lipid extract, Avanti Polar Lipids, USA) formation was used and placed in a glass-bottomed lower chamber. Mesostructured Si particles were applied into the upper bath solution and allowed to settle down to form contact with the bilayer. Laser pulses (532 nm) were delivered through a 10×/0.25 NA lens and the power was adjusted by a set of neutral density filters manually. The laser pulse frequency and duration were controlled by the in-house software and external custom-made hardware. For the capacitance measurements, the current responses of the bilayer were recorded when a 5 kHz sinusoidal carrier voltage signal was concurrently used as the voltage command, while Si-based film was illuminated by the laser pulses. For the local temperature measurements, a pipette electrode (2~4 MΩ) filled with bilayer bath solution was placed adjacent to the stimulation site. Capacitive currents were recorded in voltage-clamp mode. A laser pulse was delivered to the preparation 300 ms after the voltage was jumped from a holding potential of 0 mV to the desired voltage.

DRG neurons experiments

DRGs were extracted from P1–P3 Sprague-Dawley rats and cultured following existing protocols (See details in Supplementary Information). Mesotructured Si particles were delivered and settled onto DRG cultures. Targeted neurons with a single particle attached to the soma were patched using a ~2 MΩ pipette. Voltage recordings were made in current clamp mode. Every three seconds, a 1 ms suprathreshold amplitude current injection was delivered to the neuron to assess its excitability and followed by a 1 ms laser pulse through a

Author Manuscript

40×/0.55NA lens, 300 ms later. The minimal power enough to elicit APs was determined and applied in trains of laser pulses at different frequencies.

Supplementary Material

Refer to Web version on PubMed Central for supplementary material.

Acknowledgments

References

1. Leigh, C. Handbook of porous silicon. 1st. Springer; 2014.

2. Sailor, MJ. Porous silicon in practice: preparation, characterization, and applications. Wiley-VCH; Weinheim, Germany: 2012.

3. Kim D-H, Ghaffari R, Lu NS, Rogers JA. Flexible and stretchable electronics for biointegrated devices. Annual Review of Biomedical Engineering. 2012; 14:113–128. DOI: 10.1146/annurev-bioeng-071811-150018

4. Tian BZ, Lieber CM. Synthetic nanoelectronic probes for biological cells and tissues. Annual Review of Analytical Chemistry. 2013; 6:31–51. DOI: 10.1146/annurev-anchem-062012-092623

5. Cogan SF. Neural stimulation and recording electrodes. Annual Review of Biomedical Engineering. 2008; 10:275–309. DOI: 10.1146/annurev.bioeng.10.061807.160518

6. Tasciotti E, Liu XW, Bhavane R, Plant K, Leonard AD, Price BK, Cheng MMC, Decuzzi P, Tour JM, Robertson F, Ferrari M. Mesoporous silicon particles as a multistage delivery system for imaging and therapeutic applications. Nature Nanotechnology. 2008; 3:151–157. DOI: 10.1038/nnano.2008.34

7. Chiappini C, De Rosa E, Martinez JO, Liu X, Steele J, Stevens MM, Tasciotti E. Biodegradable silicon nanoneedles delivering nucleic acids intracellularly induce localized in vivo neovascularization. Nature Materials. 2015; 14:532–539. DOI: 10.1038/nmat4249 [PubMed: 25822693]

8. Gu L, Hall DJ, Qin ZT, Anglin E, Joo J, Mooney DJ, Howell SB, Sailor MJ. In vivo time-gated fluorescence imaging with biodegradable luminescent porous silicon nanoparticles. Nature Communications. 2013; 4

9. Kim W, Ng JK, Kunitake ME, Conklin BR, Yang P. Interfacing silicon nanowires with mammalian cells. Journal of the American Chemical Society. 2007; 129:7228–7229. DOI: 10.1021/ja071456k [PubMed: 17516647]

10. Hwang SW, Tao H, Kim DH, Cheng H, Song JK, Rill E, Brenckle MA, Panilaitis B, Won SM, Kim YS, Song YM, Yu KJ, Ameen A, Li R, Su Y, Yang M, Kaplan DL, Zakin MR, Slepian MJ, Huang

Y, Omenetto FG, Rogers JAA. Physically transient form of silicon electronics. Science. 2012; 337:1640–1644. DOI: 10.1126/science.1226325 [PubMed: 23019646]

11. Park JH, Gu L, von Maltzahn G, Ruoslahti E, Bhatia SN, Sailor MJ. Biodegradable luminescent porous silicon nanoparticles for in vivo applications. Nature Materials. 2009; 8:331–336. DOI: 10.1038/nmat2398 [PubMed: 19234444]

12. Kim DH, Viventi J, Amsden JJ, Xiao J, Vigeland L, Kim YS, Blanco JA, Panilaitis B, Frechette ES, Contreras D, Kaplan DL, Omenetto FG, Huang Y, Hwang KC, Zakin MR, Litt B, Rogers JA. Dissolvable films of silk fibroin for ultrathin conformal bio-integrated electronics. Nature Materials. 2010; 9:511–517. DOI: 10.1038/nmat2745 [PubMed: 20400953]

13. Liu J, Fu TM, Cheng Z, Hong G, Zhou T, Jin L, Duvvuri M, Jiang Z, Kruskal P, Xie C, Suo Z, Fang Y, Lieber CM. Syringe-injectable electronics. Nature Nanotechnology. 2015; 10:629–636. DOI: 10.1038/nnano.2015.115

14. Zhang AQ, Lieber CM. Nano-bioelectronics. Chemical Reviews. 2016; 116:215–257. DOI: 10.1021/acs.chemrev.5b00608 [PubMed: 26691648]

15. Zimmerman JF, Murray GF, Wang YC, Jumper JM, Austin JR II, Tian BZ. Free-standing kinked silicon nanowires for probing inter- and intracellular force dynamics. Nano Letters. 2015; 15:5492–5498. DOI: 10.1021/acs.nanolett.5b01963 [PubMed: 26192816]

16. Wegst UGK, Bai H, Saiz E, Tomsia AP, Ritchie RO. Bioinspired structural materials. Nature Materials. 2015; 14:23–36. DOI: 10.1038/nmat4089 [PubMed: 25344782]

17. Chomski E, Ozin GA. Panoscopic silicon - A material for "all" length scales. Advanced Materials. 2000; 12:1071–1078. DOI: 10.1002/1521-4095(200007)12:14<1071::aid-adma1071>3.0.co;2-j

18. Bao ZH, Weatherspoon MR, Shian S, Cai Y, Graham PD, Allan SM, Ahmad G, Dickerson MB, Church BC, Kang ZT, Abernathy HW, Summers CJ, Liu ML, Sandhage KH. Chemical reduction of three-dimensional silica micro-assemblies into microporous silicon replicas. Nature. 2007; 446:172–175. DOI: 10.1038/nature05570 [PubMed: 17344850]

19. Dai F, Zai JT, Yi R, Gordin ML, Sohn H, Chen SR, Wang DH. Bottom-up synthesis of high surface area mesoporous crystalline silicon and evaluation of its hydrogen evolution performance. Nature Communications. 2014; 5

20. Hochbaum AI, Gargas D, Hwang YJ, Yang P. Single crystalline mesoporous silicon nanowires. Nano Letters. 2009; 9:3550–3554. DOI: 10.1021/nl9017594 [PubMed: 19824705]

21. Qu Y, Liao L, Li Y, Zhang H, Huang Y, Duan X. Electrically conductive and optically active porous silicon nanowires. Nano Letters. 2009; 9:4539–4543. DOI: 10.1021/nl903030h [PubMed: 19807130]

22. Li X, Bohn PW. Metal-assisted chemical etching in HF/H(2)O(2) produces porous silicon. Applied Physics Letters. 2000; 77:2572–2574. DOI: 10.1063/1.1319191

23. Gordon LM, Cohen MJ, MacRenaris KW, Pasteris JD, Seda T, Joester D. Amorphous intergranular phases control the properties of rodent tooth enamel. Science. 2015; 347:746–750. DOI: 10.1126/science.1258950 [PubMed: 25678658]

24. Ott HC, Matthiesen TS, Goh SK, Black LD, Kren SM, Netoff TI, Taylor DA. Perfusion-decellularized matrix: using nature's platform to engineer a bioartificial heart. Nature Medicine. 2008; 14:213–221. DOI: 10.1038/nm1684

25. Gu D, Schuth F. Synthesis of non-siliceous mesoporous oxides. Chemical Society Reviews. 2014; 43:313–344. DOI: 10.1039/c3cs60155b [PubMed: 23942521]

26. Wan Y, Yang HF, Zhao DY. "Host-guest" chemistry in the synthesis of ordered nonsiliceous mesoporous materials. Accounts of Chemical Research. 2006; 39:423–432. DOI: 10.1021/ar050091a [PubMed: 16846206]

27. Arora H, Du P, Tan KW, Hyun JK, Grazul J, Xin HL, Muller DA, Thompson MO, Wiesner U. Block copolymer self-assembly-directed single-crystal homo- and heteroepitaxial nanostructures. Science. 2010; 330:214–219. DOI: 10.1126/science.1193369 [PubMed: 20929772]

28. Joo SH, Choi SJ, Oh I, Kwak J, Liu Z, Terasaki O, Ryoo R. Ordered nanoporous arrays of carbon supporting high dispersions of platinum nanoparticles. Nature. 2001; 412:169–172. DOI: 10.1038/35084046 [PubMed: 11449269]

29. Zhao DY, Feng JL, Huo QS, Melosh N, Fredrickson GH, Chmelka BF, Stucky GD. Triblock copolymer syntheses of mesoporous silica with periodic 50 to 300 angstrom pores. Science. 1998; 279:548–552. DOI: 10.1126/science.279.5350.548 [PubMed: 9438845]

30. Richman EK, Kang CB, Brezesinski T, Tolbert SH. Ordered mesoporous silicon through magnesium reduction of polymer templated silica thin films. Nano Letters. 2008; 8:3075–3079. DOI: 10.1021/nl801759x [PubMed: 18702552]

31. Tanaka, K., Maruyama, E., Shimada, T., Okamoto, H. Amorphous silicon. 1st. Wiley; 1999.

32. Freund, LB., Suresh, S. Thin film materials: stress, defect formation and surface evolution. 1st. Cambridge University Press; 2009.

33. Imperor-Clerc M, Davidson P, Davidson A. Existence of a microporous corona around the mesopores of silica-based SBA-15 materials templated by triblock copolymers. Journal of the American Chemical Society. 2000; 122:11925–11933. DOI: 10.1021/ja002245h

34. Minev IR, Musienko P, Hirsch A, Barraud Q, Wenger N, Moraud EM, Gandar J, Capogrosso M, Milekovic T, Asboth L, Torres RF, Vachicouras N, Liu Q, Pavlova N, Duis S, Larmagnac A, Voeroes J, Micera S, Suo Z, Courtine G, Lacour SP. Electronic dura mater for long-term multimodal neural interfaces. Science. 2015; 347:159–163. DOI: 10.1126/science.1260318 [PubMed: 25574019]

35. Lanzani G. Materials for bioelectronics: Organic electronics meets biology. Nature Materials. 2014; 13:775–776. DOI: 10.1038/nmat4021 [PubMed: 24952749]

36. Gautieri A, Vesentini S, Redaelli A, Buehler MJ. Hierarchical structure and nanomechanics of collagen microfibrils from the atomistic scale up. Nano Letters. 2011; 11:757–766. DOI: 10.1021/nl103943u [PubMed: 21207932]

37. Picas L, Rico F, Scheuring S. Direct measurement of the mechanical properties of lipid phases in supported bilayers. Biophysical Journal. 2012; 102:L1–L3. DOI: 10.1016/j.bpj.2011.11.4001

38. Han DX, Lorentzen JD, Weinberg-Wolf J, McNeil LE, Wang Q. Raman study of thin films of amorphous-to-microcrystalline silicon prepared by hot-wire chemical vapor deposition. Journal of Applied Physics. 2003; 94:2930–2936. DOI: 10.1063/1.1598298

39. Li L, Connors MJ, Kolle M, England GT, Speiser DI, Xiao XH, Aizenberg J, Ortiz C. Multifunctionality of chiton biomineralized armor with an integrated visual system. Science. 2015; 350:952–956. DOI: 10.1126/science.aad1246 [PubMed: 26586760]

40. Shapiro MG, Homma K, Villarreal S, Richter CP, Bezanilla F. Infrared light excites cells by changing their electrical capacitance. Nature Communications. 2012; 3

41. Carvalho-de-Souza JL, Treger JS, Dang B, Kent SBH, Pepperberg DR, Bezanilla F. Photosensitivity of neurons enabled by cell-targeted gold nanoparticles. Neuron. 2015; 86:207–217. DOI: 10.1016/j.neuron.2015.02.033 [PubMed: 25772189]

42. Sanders AW, Jeerage KM, Schwartz CL, Curtin AE, Chiaramonti AN. Gold nanoparticle quantitation by whole cell tomography. ACS Nano. 2015; 9:11792–11799. DOI: 10.1021/acsnano.5b03815 [PubMed: 26563983]

43. Liu Y, Ai K, Liu J, Deng M, He Y, Lu L. Dopamine-melanin colloidal nanospheres: An efficient near-infrared photothermal therapeutic agent for in vivo cancer therapy. Advanced Materials. 2013; 25:1353–1359. DOI: 10.1002/adma.201204683 [PubMed: 23280690]

44. Kaplan DT, Clay JR, Manning T, Glass L, Guevara MR, Shrier A. Subthreshold dynamics in periodically stimulated squid giant axons. Physical Review Letters. 1996; 76:4074–4077. DOI: 10.1103/PhysRevLett.76.4074 [PubMed: 10061185]

45. Liu Y, Ai K, Lu L. Polydopamine and its derivative materials: Synthesis and promising applications in energy, environmental, and biomedical fields. Chemical Reviews. 2014; 114:5057–5115. DOI: 10.1021/cr400407a [PubMed: 24517847]

46. Pan L, Yu G, Zhai D, Lee HR, Zhao W, Liu N, Wang H, Tee BCK, Shi Y, Cui Y, Bao Z. Hierarchical nanostructured conducting polymer hydrogel with high electrochemical activity. Proceedings of the National Academy of Sciences of the United States of America. 2012; 109:9287–9292. DOI: 10.1073/pnas.1202636109 [PubMed: 22645374]

47. Ghezzi D, Antognazza MR, Dal Maschio M, Lanzarini E, Benfenati F, Lanzani G. A hybrid bioorganic interface for neuronal photoactivation. Nature Communications. 2011; 2

48. Tee BCK, Chortos A, Berndt A, Nguyen AK, Tom A, McGuire A, Lin ZC, Tien K, Bae WG, Wang H, Mei P, Chou HH, Cui B, Deisseroth K, Ng TN, Bao Z. A skin-inspired organic digital mechanoreceptor. Science. 2015; 350:313–316. DOI: 10.1126/science.aaa9306 [PubMed: 26472906]

49. Tian BZ, Liu J, Dvir T, Jin L, Tsui JH, Qing Q, Suo Z, Langer R, Kohane DS, Lieber CM. Macroporous nanowire nanoelectronic scaffolds for synthetic tissues. Nature Materials. 2012; 11:986–994. DOI: 10.1038/nmat3404 [PubMed: 22922448]

50. Karzbrun E, Tayar AM, Noireaux V, Bar-Ziv RH. Programmable on-chip DNA compartments as artificial cells. Science. 2014; 345:829–832. DOI: 10.1126/science.1255550 [PubMed: 25124443]
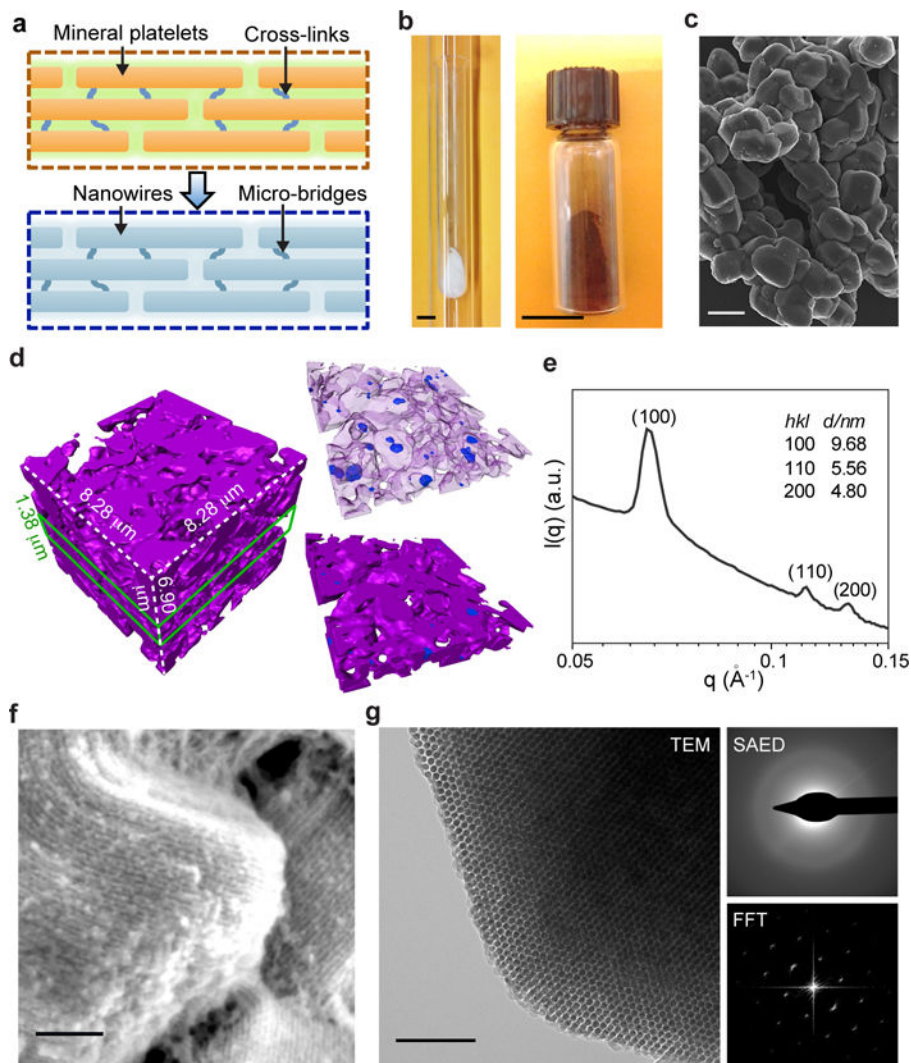
Figure 1. Amorphous Si can have multi-scale structural heterogeneity and ordered mesoscale features

a, Si-based cellular modulation materials can be designed to share similar mesostructures with natural biomaterials, *e.g.*, bones, with ordered unidirectional fibril networks that are maintained by molecular cross-links. **b**, A double quartz-tubing system was used for nano-casting synthesis, with a mesoporous SiO_2 template placed near the bottom of the inner tube (left). After HF etching, the brownish product (right) can be yielded. Scale bars, 1 cm. **c**, SEM image of as-synthesized Si particles shows a morphology similar to that of SBA-15 template. Scale bar, 2 μm. **d**, TXM 3D dataset of a representative region of mesostructured silicon (left). A thin slice of the dataset (green lines) highlights the presence of both intra- and inter-granular voids (right). Representing silicon as a semi-transparent matrix allows clearer visualization of the voids (upper right). Magenta, silicon; blue, intra-granular voids; open regions in the whole volume or thin slice, inter-granular voids. **e**, SAXS profile shows mesoscale periodicity with a 2D hexagonal symmetry. **f**, SEM image reveals periodic arrangement of Si nanowire assembly. Scale bar, 100 nm. **g**, TEM image (left) and its FFT

diffractogram (lower right) indicate the hexagonal packing of Si nanowires (left panel). SAED pattern shows an amorphous atomic structure (upper right). Scale bar, 100 nm.
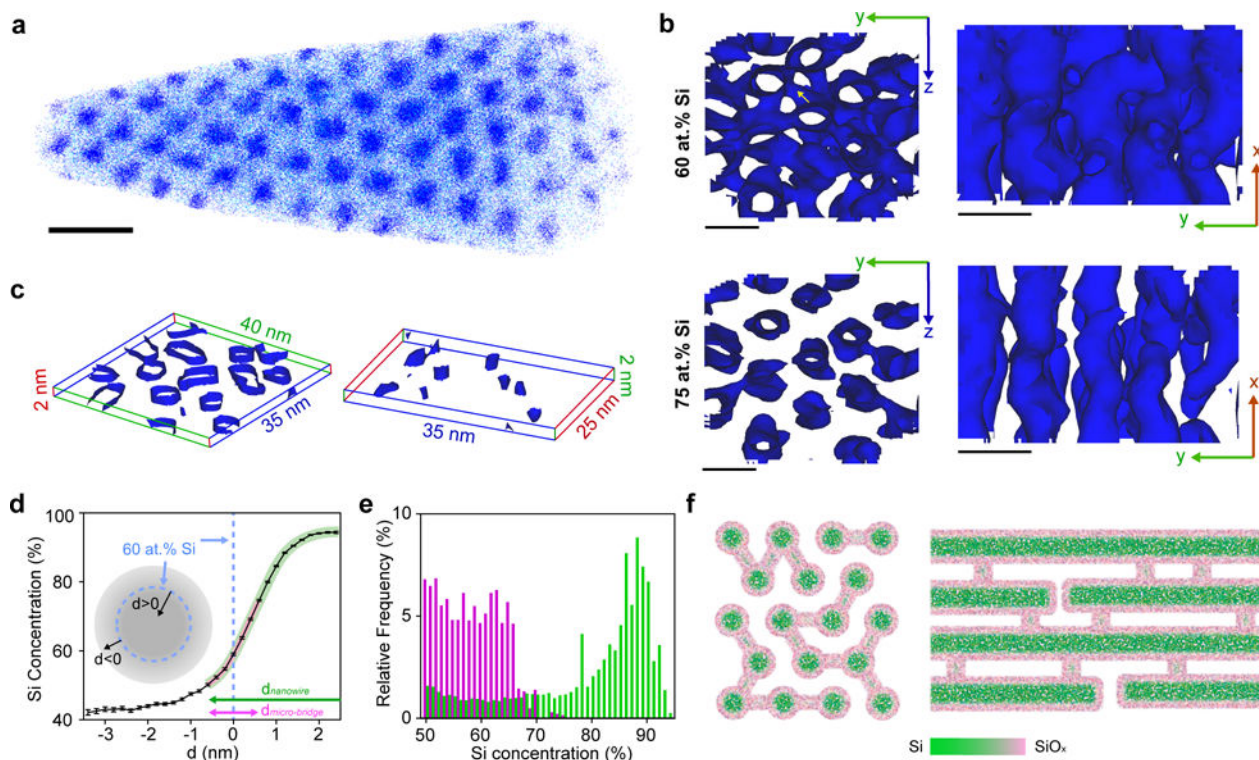
Figure 2. Mesostructured Si has size-dependent chemical heterogeneity

a, APT of one as-deposited sample (*i.e.*, without SiO_2 removal) exhibits hexagonal packing of Si nanowires in SiO_2 matrix. For clarity, only 5% of total Si (blue dots) and O (cyan dots) are displayed. Scale bar, 20 nm. **b**, 60 at.% (upper) and 75 at.% (lower) Si isoconcentration surfaces viewed from x (left) and z (right) directions. The presence of micro-bridges (yellow arrow) in 60 at.% surfaces (upper) and their absence in 75 at.% surfaces (lower) suggest that the overall Si concentration is less in micro-bridges than in Si nanowires. Scale bars, 10 nm. **c**, Representative slices showing Si nanowires (left) and micro-bridges (right) separately, rendered as 65 at.% Si isoconcentration surfaces. Lines and numbers denote dimensions along x (red), y (green) and z (blue) axes. The locations of the selected slices are marked in Supplementary Fig. S16. **d,e**, Proximity histogram concentration profiles (**d**) and Si concentration distribution histograms (**e**) confirm the size-dependent Si concentration in Si nanowires (green) and micro-bridges (pink and magenta). 'd' in **d** denotes the distance from the 60 at.% Si isoconcentration surfaces and a positive/negative value means that the point is inside/outside the enclosed isoconcentration surface. The curved pink and green thick lines estimate the decoupled Si distributions in micro-bridges and nanowires, respectively, given the different principal feature sizes in these two components (lines with arrows, magenta vs. green). **f**, End- (left) and side-view (right) schematics of mesostructured Si illustrate the graded Si/SiO_x (green/pink) interfaces and the observed chemical heterogeneity between nanowires and micro-bridges.
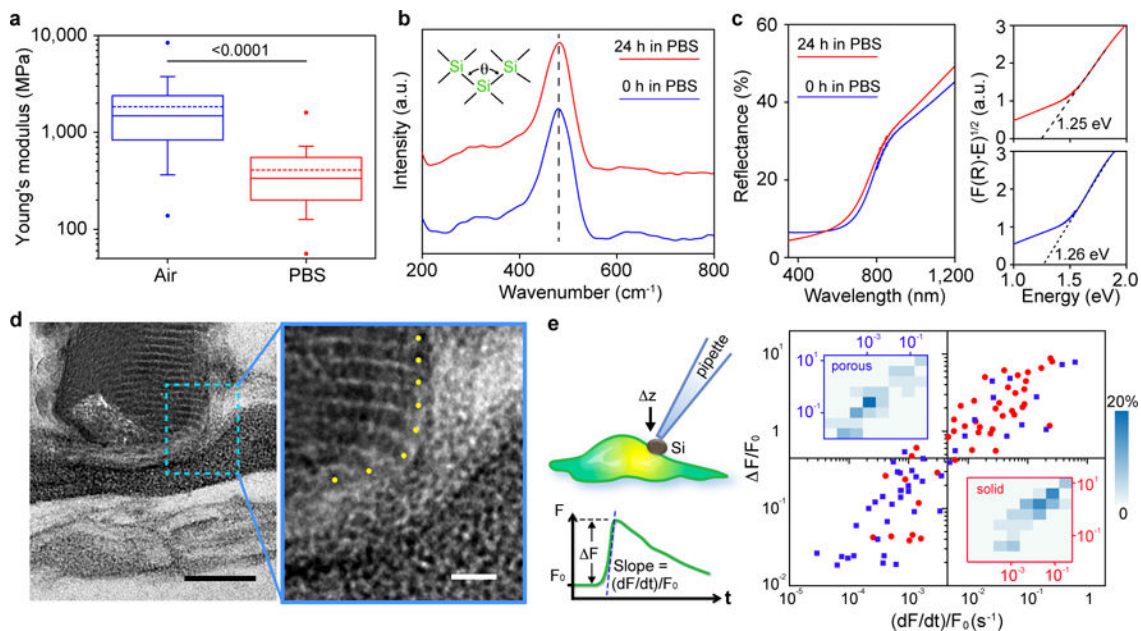
Figure 3. Mesostructured Si can establish less invasive biointerfaces

a, Box-and-whisker plot of Young's moduli of mesostructured Si measured in air (blue) and in a PBS solution (red). Half of the data points are within the boxes, 80% are within the whiskers. Solid and dashed lines represent the medians and means, respectively. The dots mark the maximum and minimum values. n=138 for measurement in air, n=94 in PBS. The number above the bar is the p-value of the Mann-Whitney test. **b,c**, Raman (**b**) and UV-vis (**c**) spectra of mesostructured Si submerged in PBS for 0 h (blue) and 24 h (red). The dashed line in **b** marks the position of Transverse Optical peak, whose position and width reflect the distribution of bond angle (θ). Extrapolation from Tauc plots (**c**, right) of the UV-vis spectra yield band gaps. $F(R)$ is the Kubelka-Munk function defined as $F(R) = (1-R)^2/2R$, where R is reflectance. E is the energy defined as $h\upsilon$. Raman and UV-vis spectra were collected in PBS and air, respectively. **d**, Cross-sectional TEM image of a representative mesostructured Si/HUVEC interface after freeze-substitution and resin embedding. Blue dashed box marks the region for a zoom-in view on the right. The nanowires ends are marked with yellow dots. Scale bars, 100 nm (left), 20 nm (right). **e**, A schematic diagram (upper left) of the single-cell calcium imaging assay, with relative amplitude ($\Delta F/F_0$) and slope (($dF/dt)/F_0$) defined (lower left). A scattered plot (right) for the amplitude and slope values of the calcium dynamics, recorded from porous/mesostructured/amorphous (blue) and solid/single crystalline (red) particles. Insets display 2D distribution histograms associated with porous (upper left) and solid (lower right) samples. $n = 44$ for each group.
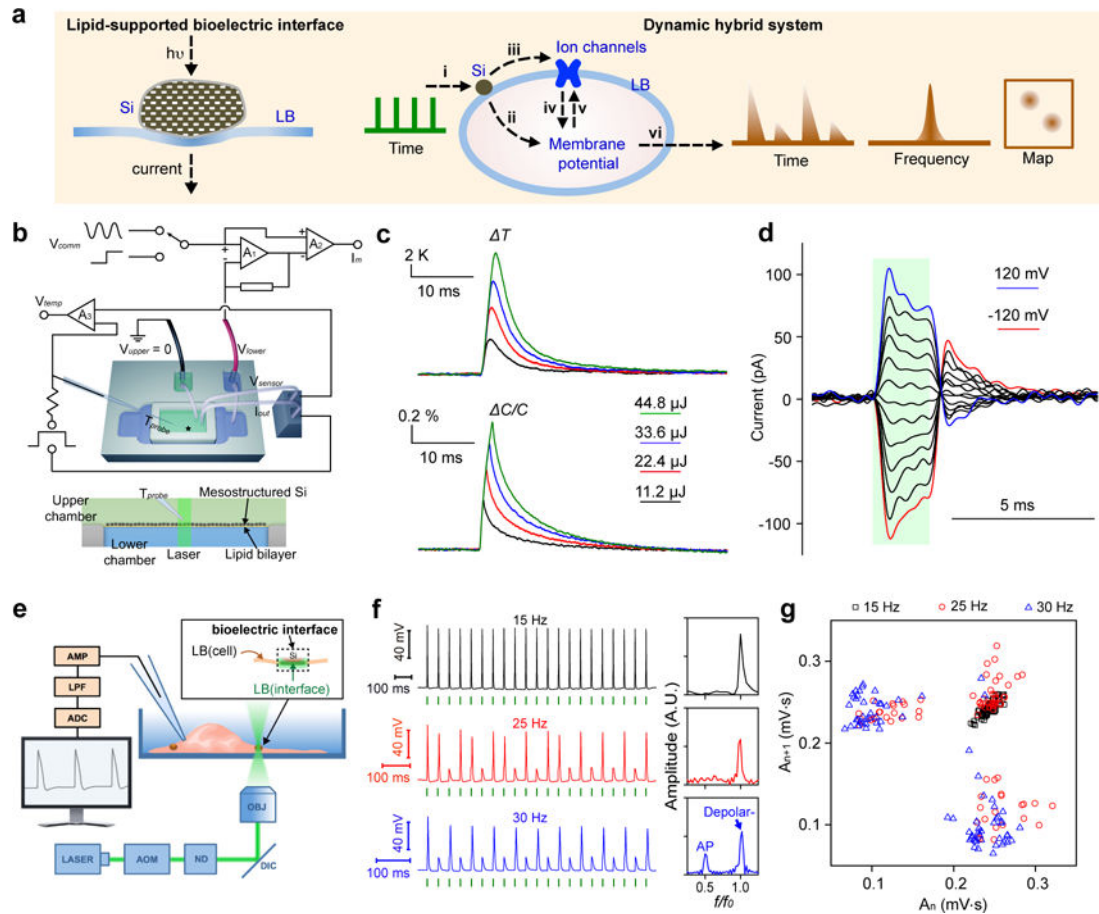
Figure 4. Remotely actuated and lipid-supported bioelectric interface as a dynamic hybrid system

a, Schematics of a light actuated bioelectric interface (left), where transient capacitive currents across lipid bilayer (LB) are generated due to the photothermal effect of mesostructured Si. A hybrid Si/cell system (right) uses pulsed optical signals as the input (**i**) and yields local transient heating. The fast transient heating generates capacitive currents through LB (**ii**) which, together with the currents passing through ion channels (**iv**), determine the membrane potential. The ion channel activities can be affected by the membrane potential (**v**) which is the result of either ionic currents and/or of the change in membrane capacitance by transient heating but also by direct heating (**iii**). All these processes integrate together as a single dynamic hybrid system, generating output (**vi**) that is recognizable in time and frequency domains and as 2D maps. **b**, A planar and remotely controlled bioelectric interface made from densely packed Si mesostructures and an artificial lipid bilayer. Experimental setup (top) shows measurements of local solution temperature, bilayer electrical capacitance, and membrane current, upon localized laser illumination at the Si/lipid interface (top panel). The star marks a drilled hole at the bottom of top chamber, where lipid bilayer forms. Two independent circuits are shown. The first circuit uses A_1 and A_2 as a patch clamp that measures membrane currents (I_m) in response to a command voltage (V_{comm}) clamped at V_{lower}, connected to the solution pool below the bilayer. V_{comm} can be conventional voltage pulses or a sinusoidal voltage signal. V_{upper} connects the pool

on top of the chamber to ground. The second circuit, using A_3, records a voltage drop (V_{temp}) between the pipette (T_{probe}) and V_{sensor}, in response to a current applied between the pipette and I_{out}. V_{temp} is proportional to the pipette resistance, which in turn is a function of the temperature (see details in the text). A zoom-in side view of the setup (bottom) shows Si/lipid interface. **c**, Averaged local solution temperature (top) and bilayer capacitance (bottom) dynamics upon laser pulses with different input energies (laser power, 22.4 mW; black, 0.5 ms; red, 1.0 ms; blue, 1.5 ms; olive, 2.0 ms). n=50. **d**, Capacitive currents in response to laser pulses (44.8μJ), recorded in voltage-clamp mode. Red and blue traces indicate the currents when the potentials were clamped at −120 mV and 120 mV, respectively. Black traces are recordings at intermediate potentials in increments of 20 mV. Green bar indicates when laser pulse was on. n=10. **e**, Experimental setup used to elicit action potentials in DRG neurons by illuminating a single Si particle attached to a cell. Neurons were patch clamped in the current-clamp whole-cell mode. AOM, acousto-optic modulator; ND, neutral density filters; DIC, dichroic mirror; OBJ, microscope objective; AMP, amplifier; LPF, low-pass filter; ADC, analog-to-digital converter. Inset shows that a portion of the cell membrane functions as a built-in bioelectric interface. **f**, Representative intracellular potential recordings of a DRG neuron to trains of laser pulses (5.32 μJ) at different frequencies, with corresponding FFTs (right). f and f_0 are output and input frequencies, respectively. Green bars indicate when laser pulses were delivered. **g**, An area-based return map reveals an evolution of frequency-dependent 2-D patterns. Data points are analyzed from 20 spikes per trial, 4 trials per frequency.